https://doi.org/10.5194/egusphere-2026-1486
Preprint. Discussion started: 24 March 2026

Sensitivity of Arctic mixed-phase cloud simulations to ice microphysical modifications in the WDM6 scheme of WRF (v4.3.1)

Hyun-Joon Sung[1], Kyo-Sun Sunny Lim[2], Song-You Hong[3], JiHoon Shin[1], Baek-Min Kim[1] and Ji-Hun Choi[1]

[1] Division of Earth Environmental System Sciences (Major of Environmental Atmospheric Sciences), Pukyong National University, 45 Yongso-ro, Nam-gu, Busan, 48513 Republic of Korea
[2] School of Earth and Environmental Sciences, Seoul National University, Seoul, Republic of Korea
[3] Mesoscale and Microscale Meteorology Laboratory (MMM), National Center for Atmospheric Research (NCAR), CO 80301, USA

Correspondence to: Baek-Min Kim (beakmin@pknu.ac.kr)

Abstract.

Arctic mixed-phase clouds (MPCs) remain challenging to represent in atmospheric models, with bulk microphysics schemes typically biased toward either excessive glaciation or inadequate ice formation. This study evaluates the behavior of the Weather Research and Forecasting (WRF) Double-Moment 6-class (WDM6) scheme and its modified version (WDM6_ICE), which incorporates spherical ice shape, constrained nucleation, and prognostic cloud ice number concentration, under Arctic conditions using the Mixed-Phase Arctic Cloud Experiment case (9–10 October 2004).

WDM6 severely underestimates liquid water through efficient vapor deposition onto bullet-shaped ice. WDM6_ICE exhibits the opposite behavior, maintaining persistent liquid as cloud ice deposition is reduced by approximately 98%. The suppressed cloud ice is partially compensated by enhanced snow deposition, resulting in a 60–80% reduction of total ice water content rather than complete ice elimination. Sensitivity experiments show that ice shape modification is the dominant factor, while nucleation modification alone redistributes ice among hydrometeor categories without reducing total ice content. Comparison with mid-latitude evaluations of the same scheme reveals a regime-dependent response: modifications that produce moderate ice adjustment in mid-latitude cases lead to a fundamental restructuring of the ice budget under Arctic conditions.Surface energy analysis indicates that balanced phase partitioning is more relevant than liquid water maximization for radiative bias reduction. All configurations underestimate total water path, suggesting that accurate Arctic MPC representation requires coordinated improvements in ice particle properties, ice-nucleating particle recycling, and boundary-layer coupling.

1 Introduction

The representation of mixed-phase cloud (MPC) processes remains a persistent challenge for cloud microphysics parameterizations. This challenge is particularly evident in the Arctic, where MPCs exhibit remarkable persistence despite the thermodynamic instability associated with the coexistence of supercooled liquid and ice (Morrison et al., 2020, 2012).

https://doi.org/10.5194/egusphere-2026-1486
Preprint. Discussion started: 24 March 2026

Most bulk microphysics schemes produce either excessive ice or excessive liquid under Arctic conditions, rarely achieving the observed balanced mixed-phase state (Klein et al., 2009; Morrison et al., 2009; Possner et al., 2024). These systematic biases reflect fundamental difficulties in parameterizing the competition for water vapor between ice and liquid phases, the coupling between cloud microphysics and boundary-layer turbulence, and the sensitivity of phase partitioning to ice nucleation and growth assumptions (Shupe and Intrieri, 2004; Morrison and Pinto, 2006; Turner et al., 2007)

Among the bulk microphysics schemes available in the Weather Research and Forecasting (WRF) model, the Double-Moment 6-Class (WDM6) scheme (Lim and Hong, 2010) is widely used for cloud and precipitation forecasting. WDM6 diagnoses cloud ice number concentration from ice mixing ratio and assumes bullet-shaped cloud ice with ice nucleation following the Hong et al. (2004), Unlike double-moment schemes such as Morrison et al. (2005) and Thompson et al. (2008) that predict ice number concentration prognostically, the diagnostic treatment in WDM6 creates tight coupling between ice mass and number concentration, preventing independent evolution of particle size distributions. These structural characteristics lead to distinct ice representation behavior compared with other microphysics schemes in mid-latitude environments (Comin et al., 2018; McMillen and Steenburgh, 2015). In the Arctic, WDM6 shows smaller biases in ice water content (IWC) but significantly underestimates supercooled liquid water (Nam et al., 2024), highlighting the complex regional dependencies in scheme performance.

To improve the ice representation in WDM6, the WDM6_ICE scheme (Park and Lim, 2023) incorporates three key modifications: prognostic cloud ice number concentration, spherical cloud ice shape, and updated ice nucleation parameterizations based on the Cooper (1986) curve with an observationally constrained upper limit (DeMott et al., 2010). WDM6_ICE also includes additional ice-phase processes such as contact freezing, enhanced riming, and secondary ice production via the Hallett–Mossop mechanism. These modifications were developed and validated using mid-latitude precipitation cases over the Korean Peninsula, where they reduced cloud ice mixing ratio and produced mixed improvements in precipitation skill scores.

Cloud microphysics parameterizations are typically developed and validated within specific climate regimes. While their overall performance has been evaluated across diverse environments, how individual microphysical modifications respond to fundamentally different environmental conditions has received less attention. Whether microphysical corrections optimized for one regime maintain their physical validity under fundamentally different conditions remains an open question. This concern is particularly relevant for ice microphysics modifications, where the balance between ice and liquid phases depends jointly on the temperature range, aerosol availability, boundary-layer structure, and moisture supply, all of which vary substantially across climate regimes. Parameterizations that successfully correct ice overproduction in mid-latitude systems, for example, may produce qualitatively different responses in shallow Arctic stratiform clouds where temperature ranges are narrow, ice-nucleating particle concentrations are low, and boundary-layer coupling plays a dominant role in cloud maintenance (Fridlind et al., 2012; Morrison et al., 2012).

This study evaluates the behavior of WDM6 and WDM6_ICE under Arctic conditions using the Mixed-Phase Arctic Cloud Experiment (M-PACE) case observed on 9–10 October 2004. M-PACE provides a well-documented benchmark for

https://doi.org/10.5194/egusphere-2026-1486
Preprint. Discussion started: 24 March 2026

evaluating microphysics schemes in the Arctic, with studies consistently identifying challenges in ice nucleation representation (Fridlind et al., 2007), liquid water maintenance (Klein et al., 2009; Luo et al., 2008), secondary ice production (Possner et al., 2024), and ice shape sensitivity (Ong et al., 2024). The study aims to: (1) evaluate the cloud phase partitioning produced by WDM6 and WDM6_ICE under Arctic conditions; (2) decompose the contributions of ice shape and nucleation modifications to the phase partitioning transition through controlled sensitivity experiments; and (3) elucidate the feedback mechanisms that govern the sensitivity of Arctic cloud phase partitioning to these structural modifications, including the additional effect of prognostic ice number treatment inferred from comparison between WDM6_SP_IN and the full WDM6_ICE scheme.

2 Data and Methods

2.1 Data

This study uses aircraft measurements and surface-based observational datasets to evaluate simulations of Arctic MPCs. Aircraft observations were obtained from the M-PACE campaign. Specifically, this study analyzes measurements from Flight 10a, conducted on 10 October 2004. While the flight track extended along the northern coast of Alaska (Fig. S1), the analysis focuses on the segment collected between 01:10-02:00 UTC over Barrow (BAR), consistent with Fu et al. (2019). These aircraft observations provide a comprehensive in situ microphysics dataset (McFarquhar et al., 2007) containing quality-controlled estimates of IWC, liquid water content (LWC), effective radius, and number concentration for both liquid and ice phases. McFarquhar et al. (2007) reported that the observed ice particles included a variety of habits such as columns, plates, bullet rosettes, and heavily rimed particles, with graupel also present particularly near cloud base. The observed IWC and number concentration represent the combined contribution from all ice-phase particles, as aircraft probes measure a continuous size distribution without distinguishing model-specific hydrometeor categories.

Surface measurements at BAR were derived from the Department of Energy (DOE) Atmospheric Radiation Measurement (ARM) North Slope of Alaska (NSA) facility. To characterize atmospheric and cloud properties, the following ARM data products were utilized: ARM Best Estimate Atmospheric Measurements (ARMBEATM) for 2-meter air temperature (T2M), Microwave Radiometer Retrievals (MWRRET) for liquid water path (LWP), and Quality Controlled Radiation (QCRAD) value-added product for surface radiative fluxes (downward shortwave radiation, SWDOWN; downward longwave radiation, LWDOWN).lce water path (IWP) was obtained from the multisensor Arctic Cloud Radiative Effects Dataset (ACRED). Additionally, radiosonde profiles at BAR were used to evaluate the vertical moisture structure of ERA5 boundary conditions (Fig. S3).

https://doi.org/10.5194/egusphere-2026-1486
Preprint. Discussion started: 24 March 2026

2.2 Case description

The M-PACE campaign was conducted in autumn 2004 to investigate the characteristics and processes of Arctic MPCs. The campaign was based at BAR (Verlinde et al., 2007) and provided extensive observations describing the microphysics, radiative effects, and life cycle of these clouds. The observed clouds were predominantly stratiform MPCs containing both supercooled liquid water and ice (McFarquhar et al., 2007; Shupe et al., 2008). During the analysis period, a single-layer MPC embedded in the boundary layer was observed over the study region.

ECMWF Reanalysis 5 (ERA5) at 00 UTC 9 October 2004 shows a strong low-pressure system near the Bering Sea coast of southern Alaska (Fig. 1a). This system interacted with a high-pressure region extending from the Chukchi Sea toward Alaska, creating a pronounced pressure gradient over the study region. The synoptic configuration drove cold air (below −6 °C) from the pack ice southward over the relatively warm open ocean (above 0 °C), establishing a strong temperature gradient. The high-pressure system formed over the pack ice on 4 October and persisted until 15 October, maintaining this advection pattern. As the sea ice edge advanced southward, the cooled air reached the Alaskan coast, triggering roll-cloud formation visible in satellite imagery (Fig. 1b). Detailed synoptic-scale characteristics for this period are described in Solomon et al. (2009) and Verlinde et al. (2007).

This persistent stratocumulus system presents fundamental challenges for numerical models, particularly regarding maintaining supercooled liquid water in the presence of ice, accurate representation of ice–liquid partitioning, and capturing cloud persistence under Arctic boundary-layer conditions. These characteristics make this event an ideal case for evaluating the performance of ice microphysics modifications in the WDM6 scheme under Arctic environments.

https://doi.org/10.5194/egusphere-2026-1486
Preprint. Discussion started: 24 March 2026

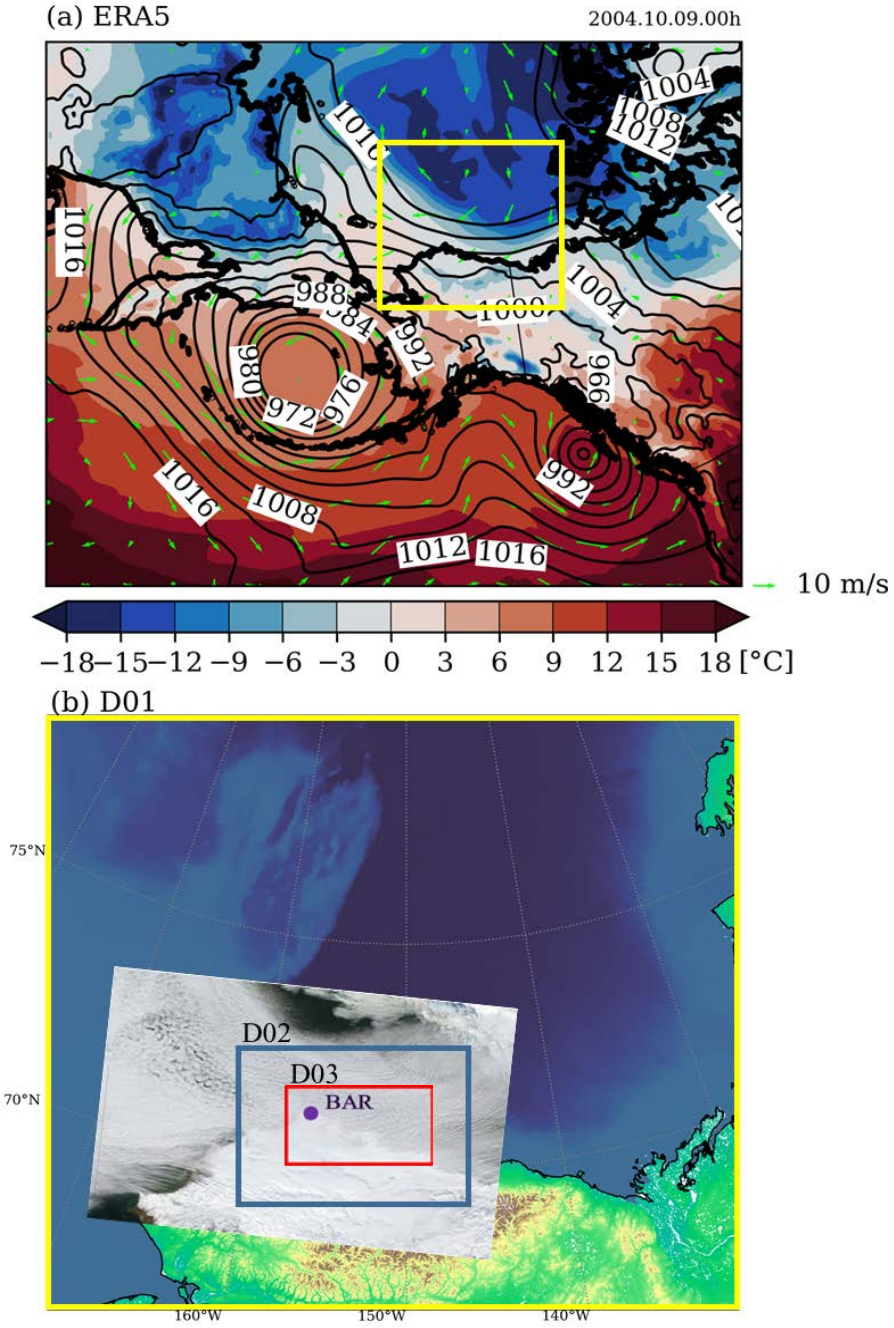

Figure 1: (a) ERA5 data showing sea level pressure (contours), 2-meter temperature (shading), and 10-m wind (vectors) at 00:00 UTC 9 October 2004. The yellow box indicates the WRF model domain (D01). (b) Nested model domains with D01 (18-km resolution), D02 (6-km resolution), and D03 (1-km resolution). The MODIS visible image shows the Arctic Ocean and northern Alaska at 00:00 UTC 9 October 2004. The location of Barrow (BAR) observation sites is marked.

https://doi.org/10.5194/egusphere-2026-1486
Preprint. Discussion started: 24 March 2026

2.3 Experimental setup

The simulations were performed using the WRF model version 4.3.1 (Skamarock Wet al., 2021). The model integrated for the period 8-10 October 2004 to simulate the M-PACE case, with the initial 24 hours serving as a spin-up period to establish stable atmospheric conditions independent of initial conditions. The analysis focused on the subsequent 24-hour period (12:00 UTC 9 October – 11:00 UTC 10 October 2004). The horizontal grid spacing for the domains is set at 18 km, 6 km, and 1 km, following the configuration of Solomon et al. (2009). Initial and boundary conditions were obtained from ERA5 data (Hersbach et al., 2020). The vertical structure includes 50 levels with enhanced boundary layer resolution, including 20 levels below 800 hPa (Table 1).

Table 1: Description of the WRF configuration used in the model experiments.

Configuration	Description
Simulation period	12:00 UTC 8 October 2004 – 12:00 UTC 10 October 2004 (spin up time: 12:00 UTC 8 October 2004 – 11:00 UTC 9 October 2004)
Horizontal grid spacing	18 km, 6 km, 1 km
Vertical layers	50 layers (model top: 50 hPa) 20 layers (model bottom to 800 hPa)
Vertical coordinate	Hybrid vertical coordinate
Time step	60 s, 20 s, 3.33 s
Radiation	RRTMG scheme (Iacono et al., 2008)
Land surface physics	Unified Noah land-surface model (Chen and Dudhia, 2001)
Surface layer physics	Revised MM5 Monin-Obukhov scheme (Jiménez et al., 2012)
Planetary boundary layer (PBL) mixing	YSU PBL scheme (Hong et al., 2006)
Initial and boundary data	ECMWF Reanalysis 5 (ERA5) data (Hersbach et al., 2020)
CCN initialization	100 cm^{-3}, uniform; prognostic with minimum floor of 100 cm^{-3} enforced at each timestep

Model outputs were extracted using two distinct approaches for validation. For surface-based validation, the WRF tslist utility was used to extract data at the grid point nearest to the BAR observation site, ensuring spatial consistency with ground measurements. For comparison with aircraft observations, model outputs were sampled along the flight region within the innermost domain (D03), capturing the representative cloud microphysical properties coincident with the flight path. Following Solomon et al. (2009), model IWC is calculated as the sum of cloud ice, snow, and graupel mixing ratios to

https://doi.org/10.5194/egusphere-2026-1486
Preprint. Discussion started: 24 March 2026

ensure consistency with aircraft observations, which measure the total ice-phase size distribution without distinguishing model-specific hydrometeor categories.

The WDM6 (Lim and Hong, 2010) and WDM6_ICE (Park and Lim, 2023) microphysics schemes served as the primary comparison pair. WDM6_ICE incorporates spherical ice shape, modified ice nucleation, and prognostic cloud ice number concentration. It also includes additional ice-enhancing processes such as contact freezing (Cotton et al., 1986), enhanced riming efficiency (Pruppacher and Klett, 2010), and secondary ice production via the Hallett–Mossop mechanism (Hallett and Mossop, 1974).

Three additional sensitivity experiments were designed to decompose the individual and combined effects of ice shape and nucleation modifications (Table 2). Since the WDM6_ICE scheme incorporates multiple processes alongside structural changes, this study isolates the two factors most directly responsible for constraining ice growth: ice particle geometry and INP availability. Secondary ice production and other ice-multiplying mechanisms were excluded from the sensitivity decomposition to avoid compensating interactions that would obscure the primary drivers of phase partitioning changes. The complete microphysical formulation of WDM6_ICE is documented in Park & Lim (2023), with key modifications summarized in Appendix A.

Table 2: Experiments description.

Experiments	Description
WDM6	WDM6 (Lim and Hong, 2010)
WDM6_ICE	Revised WDM6 scheme proposed by Park & Lim (2023). - Spherical ice shape, modified nucleation, prognostic cloud ice number concentration and additional ice microphysics - Key modifications in Appendix A; complete formulation in Park & Lim (2023)
WDM6_SP	WDM6 with a spherical cloud ice shape assumption - Adopts the geometric configuration used in WDM6_ICE. - Mass-dimension relationship follows the spherical approximation (originally derived from observations by (Brown and Francis, 1995; Korolev and Isaac, 2003)
WDM6_IN	WDM6 with modified ice nucleation parameterization - Adopts the nucleation parameterization used in WDM6_ICE. - INP number concentration of Cooper, (1986) and its limitation of DeMott et al., (2010)
WDM6_SP_IN	WDM6 with both spherical shape and ice nucleation modifications - All modifications in WDM6_SP - All modifications in WDM6_IN

https://doi.org/10.5194/egusphere-2026-1486
Preprint. Discussion started: 24 March 2026

WDM6_SP isolates the impact of cloud ice shape. The spherical assumption implies a higher effective density compared to the bullet shape in WDM6. For a given ice mass, this results in a smaller effective diameter and capacitance, which reduces the vapor depositional growth rate (Pruppacher and Klett, 2010). WDM6_IN isolates the impact of ice nucleation. The default parameterization in WDM6 (Hong et al., 2004) diagnoses INP number concentration as an exponential function of temperature. WDM6_IN adopts the Cooper curve (Cooper, 1986) with an upper limit of 500 L^{-1} (DeMott et al., 2010), which restricts INP number concentration at temperatures warmer than approximately −22 °C relative to WDM6. WDM6_SP_IN combines both modifications to examine potential non-linear interactions between particle growth efficiency and number concentration constraints. Since WDM6_SP_IN and WDM6_ICE share the same ice shape and nucleation formulations but differ in ice number treatment (diagnostic vs. prognostic) and in the inclusion of additional processes (contact freezing, Hallett–Mossop mechanism, and temperature threshold for vapor deposition nucleation; see Appendix A3), their comparison provides an indication of how these remaining structural differences affect the overall phase partitioning.

https://doi.org/10.5194/egusphere-2026-1486
Preprint. Discussion started: 24 March 2026

3 Results

3.1 Spatial and Vertical Cloud Structure in WDM6 and WDM6_ICE

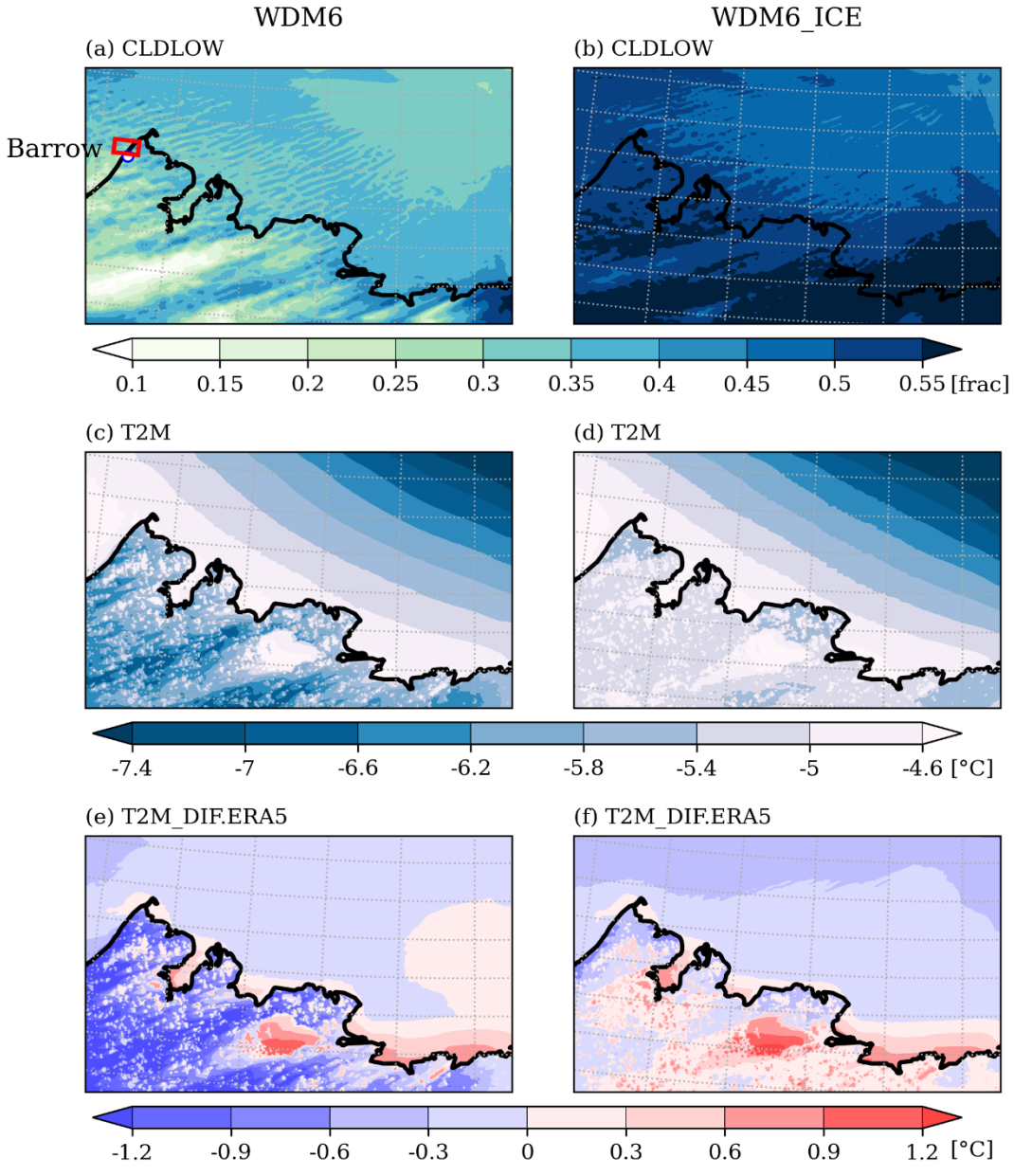

Figure 2: Time-averaged (12:00 UTC 9 October – 11:00 UTC 10 October 2004) spatial distributions from (left column) WDM6 and (right column) WDM6_ICE simulations: (a, b) low-level cloud fraction (CLDLOW; below 1500 m), (c, d) T2M, and (e, f) T2M differences (simulation – ERA5). The red box in (a) indicates the flight track area during the analysis period (01:00–02:00 UTC 10 October 2004).

https://doi.org/10.5194/egusphere-2026-1486
Preprint. Discussion started: 24 March 2026

WDM6 produces limited low-level cloud fractions (0.1–0.3) across domain D03, with slightly higher values along the coastal regions (Fig. 2a). These low cloud fractions correspond to widespread cold T2M (−7.0 °C to −6.6 °C), with the coldest values occurring in cloud-free areas (Fig. 2c). In contrast, WDM6_ICE exhibits substantially higher cloud fractions (0.4–0.55), with more uniform coverage extending into regions that are cloud-free in WDM6 (Fig. 2b). The increased cloud fraction is associated with warmer T2M ranging from −5.9 °C to −5.5 °C (Fig. 2d).

The T2M bias patterns relative to ERA5 illustrate the regional impact of these cloud differences (Fig. 2e, f). WDM6 exhibits predominantly negative biases (−1.2 °C to −0.3 °C) across the domain, while WDM6_ICE shows smaller negative biases (−0.7 to 0 °C). Point-based validation at the BAR observation site confirms this pattern, with T2M bias decreasing from −1.3 °C in WDM6 to −0.9 °C in WDM6_ICE relative to the observed mean of −4.6 °C.

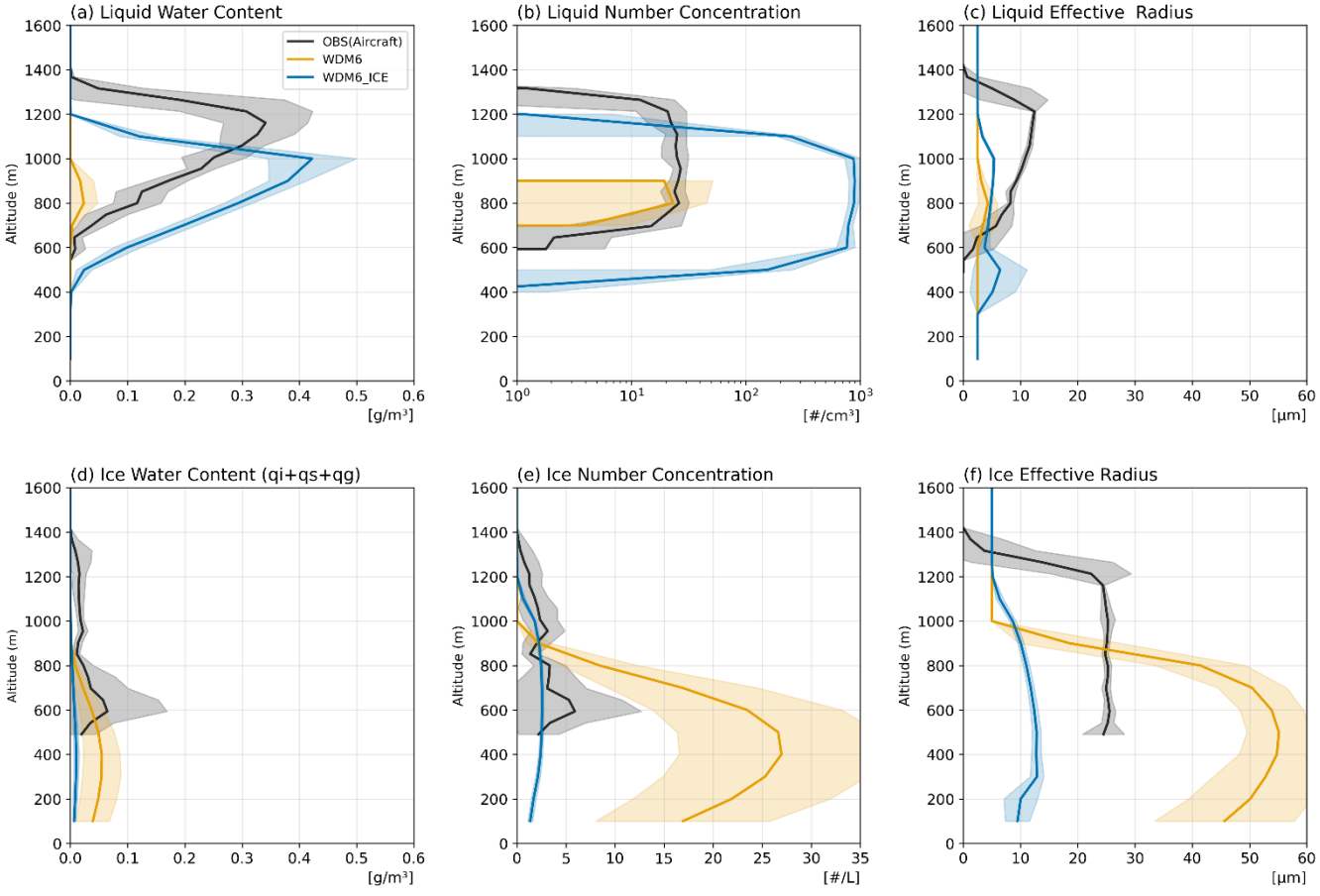

Figure 3: Vertical profiles of cloud microphysical properties spatially averaged over the flight track (Flight 10a). Panels show (a-c) liquid water content (LWC), number concentration, and effective radius, and (d-f) ice water content (IWC), number concentration, and effective radius. Black lines represent aircraft observations (01:10-02:00 UTC 10 October 2004) with gray shading indicating ±1 standard deviation (σ). Colored lines denote model simulations averaged over 01:00-02:00 UTC, WDM6 (orange) and WDM6_ICE (blue) with shading indicating ±1 σ.

https://doi.org/10.5194/egusphere-2026-1486
Preprint. Discussion started: 24 March 2026

To evaluate the simulated vertical hydrometeor structure, model results were spatially averaged over the flight region and compared with aircraft observations (Fig. 3). The observations show a liquid-dominated mixed-phase cloud. LWC peaks at 0.34 g m^{-3} around 1150 m, whereas IWC remains below 0.1 g m^{-3} throughout the cloud layer (Fig. 3a, d). Liquid droplets are characterized by moderate number concentrations (17–27 cm^{-3}) and effective radii of 8–12 µm (Fig. 3b, c). Ice particles are sparse (mean ~2.4 L^{-1}, peak <6 L^{-1}) with effective radii of ~22 µm (Fig. 3e, f).

WDM6 produces an ice-dominated vertical structure. The simulation generates minimal LWC (peak ≈ 0.02 g m^{-3} at 800 m) while maintaining substantial IWC (~0.055 g m^{-3}). Total ice number concentration reaches ~27 L^{-1} (mean ~10.5 L^{-1}), exceeding observations by approximately fourfold, with cloud ice dominating the number budget (mean ~17.4 L^{-1}) and snow (~0.6 L^{-1}) and graupel (~0.1 L^{-1}) contributing minimally (Fig. 3e). Cloud ice effective radius ranges from 5 to 55 µm, with mean values (~27 µm) comparable to observations (~22 µm) (Fig. 3f). The liquid phase remains restricted, exhibiting low number concentrations (<23 cm^{-3}) and small droplet sizes (3–4 µm). WDM6_ICE reproduces the observed liquid-dominated structure, with simulated LWC peaking at 0.42 g m^{-3} around 1000 m, closely matching the observed magnitude (Fig. 3a). However, WDM6_ICE simulates substantially higher liquid number concentrations (reaching ~890 cm^{-3}; Fig. 3b), exceeding observations (~27 cm^{-3}) by more than an order of magnitude, with correspondingly small effective radii (2.5–6.4 µm; Fig. 3c) well below observed values (8–12 µm). Total IWC is substantially reduced relative to both WDM6 and observations, with peak values of approximately 0.01 g m^{-3} (Fig. 3d). The residual ice content is maintained primarily through the snow category rather than cloud ice. The total ice number concentration (~1.3 L^{-1}; Fig. 3e) is low but within the same order of magnitude as observations (~2.4 L^{-1}). The ice number budget in WDM6_ICE is dominated by snow (~1.0 L^{-1}) rather than cloud ice (~0.3 L^{-1}), whereas in WDM6 cloud ice dominates. Cloud ice effective radius is small (5–13 µm; Fig. 3f). Note that the effective radius comparison is limited to the cloud ice category only; the structural implications of this constraint are discussed in Section 4.4.

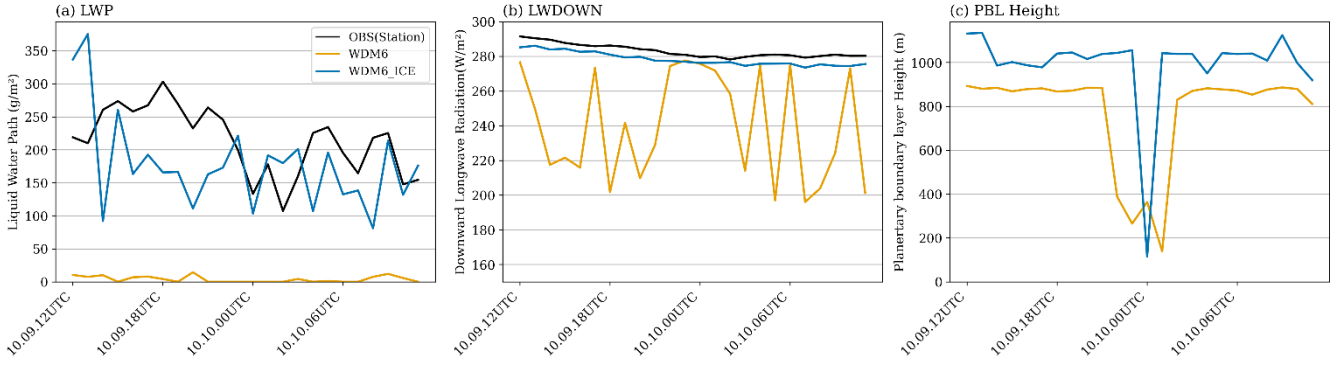

Figure 4: Time series (12:00 UTC 9 October – 11:00 UTC 10 October 2004) at BAR of (a) liquid water path (LWP), (b) downward longwave radiation (LWDOWN), and (c) planetary boundary layer (PBL) height. Black lines: observations; orange lines: WDM6; blue lines: WDM6_ICE.

At BAR, observations indicate persistent liquid-containing clouds throughout the 24-hour period, with LWP averaging 214.5 g m^{-2} (Fig. 4a). WDM6 exhibits intermittent behavior with sporadic peaks reaching 14.5 g m^{-2} and a period average of only

https://doi.org/10.5194/egusphere-2026-1486
Preprint. Discussion started: 24 March 2026

3.8 g m^{-2}. WDM6_ICE maintains a continuous liquid phase averaging 178.1 g m^{-2}. LWDOWN shows corresponding differences (Fig. 4b): observed values remain stable near 283.0 W m^{-2}, WDM6 produces 239.8 W m^{-2}, and WDM6_ICE reproduces 278.4 W m^{-2}. PBL height also differs, with WDM6 simulating 775.4 m and WDM6_ICE producing 992.3 m (Fig. 4c).

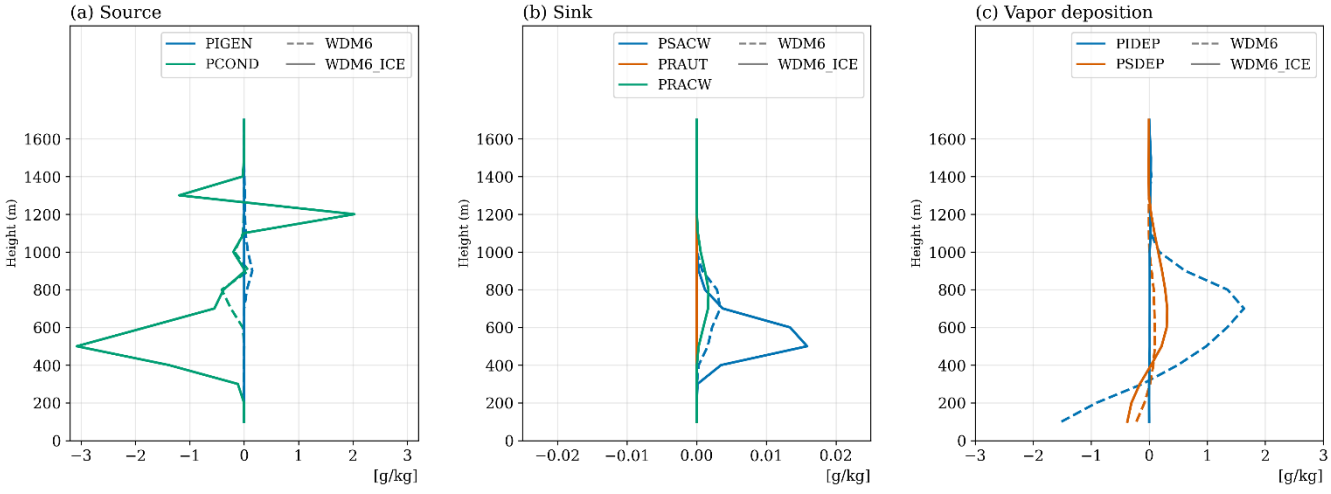

Figure 5: Time-averaged (12:00 UTC 9 October – 11:00 UTC 10 October 2004) vertical profiles of microphysical process rates at BAR: (a) Source terms (PIGEN: blue, PCOND: green), (b) Sink terms (PSACW: blue, PRAUT: vermillion, PRACW: green), and (c) Vapor deposition terms (PIDEP: blue, PSDEP: vermillion). Dashed lines represent WDM6, and solid lines represent WDM6_ICE. Note that negative values in (a) indicate evaporation.

Vertical profiles of microphysical process rates show distinct distributions between the two schemes (Fig. 5). Ice generation (PIGEN) reaches 0.15 g kg^{-1} h^{-1} in WDM6 while remaining near zero in WDM6_ICE (Fig. 5a). Conversely, liquid condensation (PCOND) is suppressed in WDM6 (<0.08 g kg^{-1} h^{-1}), whereas in WDM6_ICE PCOND dominates as the primary source term, exceeding 2.0 g kg^{-1} h^{-1}.

WDM6 exhibits minimal accretion of cloud liquid by snow (PSACW < 0.003 g kg^{-1} h^{-1}; Fig. 5b), consistent with the low liquid water content shown in Figure 3a. WDM6_ICE shows PSACW reaching 0.016 g kg^{-1} h^{-1}, a five-fold increase. Note that this elevated PSACW transfers mass from the liquid to snow category rather than to cloud ice, so it does not contradict the reduced IWC in WDM6_ICE. Rain mixing ratio is negligible in both simulations throughout the analysis period (not shown).

Deposition onto cloud ice (PIDEP) dominates in WDM6, with peak rates of 1.6 g kg^{-1} h^{-1} (Fig. 5c). In WDM6_ICE, PIDEP remains below 0.03 g kg^{-1} h^{-1}, representing an approximate 98% reduction. Deposition onto snow (PSDEP) increases threefold in WDM6_ICE, from 0.1 to 0.31 g kg^{-1} h^{-1}.

https://doi.org/10.5194/egusphere-2026-1486
Preprint. Discussion started: 24 March 2026

3.3 Sensitivity to Individual Microphysical Modifications

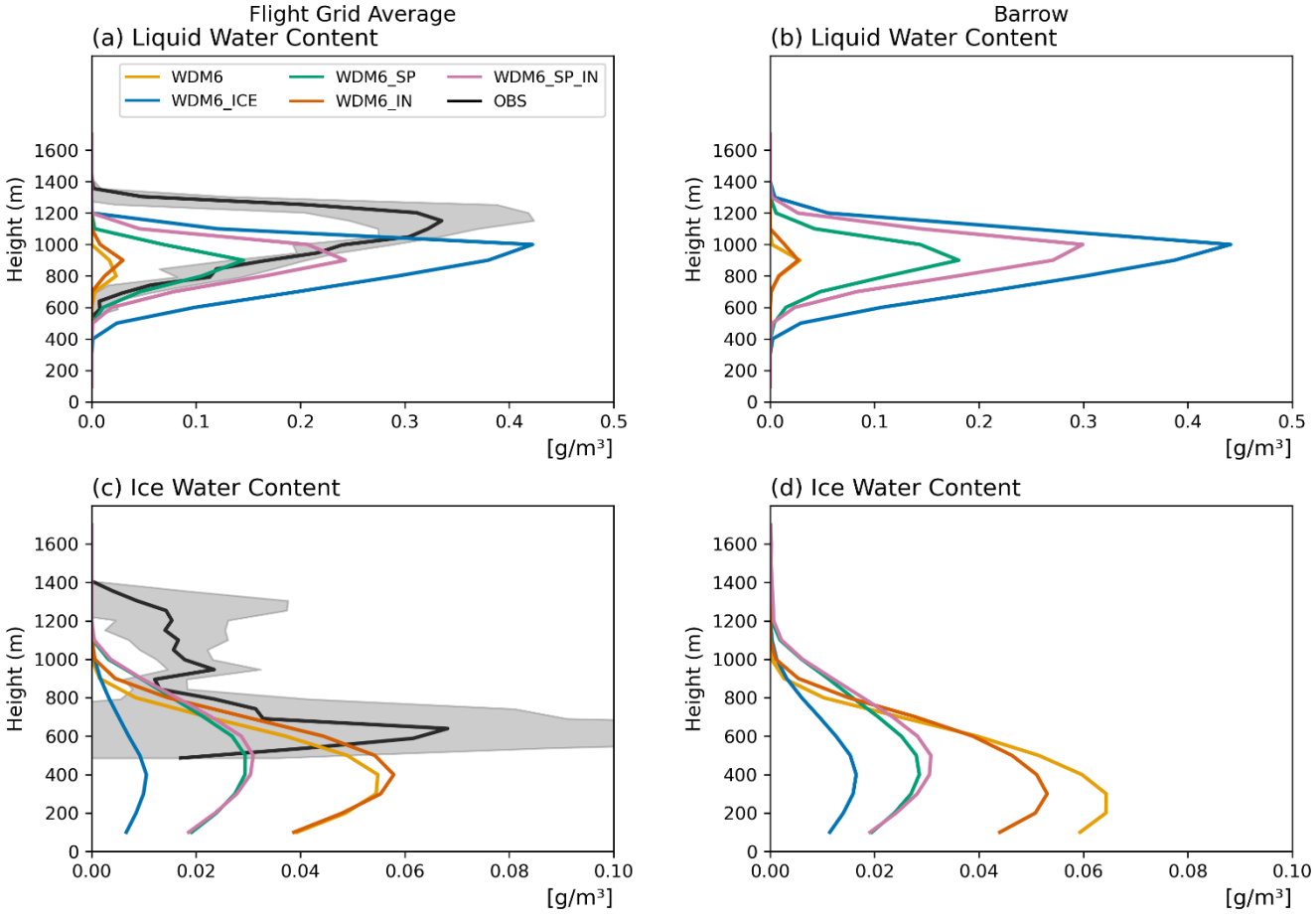

Figure 6: Vertical profiles of (a, b) LWC and (c, d) IWC. The left column (a, c) shows the spatially averaged profile over the flight region (red box in Fig. 2a) during 01:00–02:00 UTC 10 October 2004, and the right column (b, d) shows the time-averaged (12:00 UTC 9 October – 11:00 UTC 10 October 2004) profile at BAR. Black lines with gray shading indicate observations (±1σ), and colored lines represent sensitivity experiments: WDM6 (orange), WDM6_ICE (blue), WDM6_SP (green), WDM6_IN (vermillion), and WDM6_SP_IN (purple).

The sensitivity experiments show systematic differences in cloud phase partitioning (Fig. 6). LWC increases in the order WDM6 < WDM6_IN < WDM6_SP < WDM6_SP_IN < WDM6_ICE (Fig. 6a, b). The IWC response is more complex: ice shape modification (WDM6_SP) substantially reduces IWC, whereas nucleation modification alone (WDM6_IN) produces IWC comparable to WDM6, suggesting that the Cooper curve redistributes ice among hydrometeor categories rather than reducing total ice content (Fig. 6c, d).

Over the aircraft sampling region, WDM6_SP increases peak LWC to 0.15 g m^{-3} compared to 0.02 g m^{-3} in WDM6 (Fig. 6a). WDM6_IN produces minimal enhancement, reaching 0.03 g m^{-3}. WDM6_SP_IN combines both modifications, yielding

https://doi.org/10.5194/egusphere-2026-1486
Preprint. Discussion started: 24 March 2026

0.24 g m^{-3}. WDM6_ICE reaches 0.42 g m^{-3}. For IWC, WDM6 produces approximately 0.05 g m^{-3}, comparable to observations (~0.07 g m^{-3}; Fig. 6c). WDM6_SP and WDM6_SP_IN reduce IWC to approximately 0.03 g m^{-3}, while WDM6_IN maintains IWC near the WDM6 level (~0.06 g m^{-3}). WDM6_ICE reduces IWC to approximately 0.01 g m^{-3}, representing an approximately 80% reduction relative to WDM6.Time-averaged profiles at BAR demonstrate similar progression (Fig. 6b, d). WDM6_SP_IN produces peak LWC of 0.30 g m^{-3}, intermediate between WDM6_SP (0.18 g m^{-3}) and WDM6_ICE (0.44 g m^{-3}). The corresponding IWC decreases to approximately 0.03 g m^{-3} in WDM6_SP_IN compared to approximately 0.06 g m^{-3} in WDM6.

Table 3: Time-averaged (12:00 UTC 9 October – 11:00 UTC 10 October 2004) surface variables (SWDOWN, LWDOWN, T2M), column-integrated variables (IWP, LWP) at BAR. OBS values are from ground-based measurements.

Barrow	SWDOWN (W m^{-2})	LWDOWN (W m^{-2})	IWP (g m^{-2})	LWP (g m^{-2})	T2M (°C)
OBS	13.0	283.0	31.5	214.5	−4.6
WDM6	25.9	239.8	38.0	3.8	−5.9
WDM6_ICE	8.7	278.4	10.6	178.1	−5.5
WDM6_SP	20.8	272.9	20.8	55.7	−5.4
WDM6_IN	25.9	244.1	33.5	5.0	−5.8
WDM6_SP_IN	13.9	277.2	22.5	103.5	−5.4

SWDOWN and LWDOWN vary systematically across experiments. SWDOWN decreases from 25.9 W m^{-2} (WDM6) to 8.7 W m^{-2} (WDM6_ICE), while LWDOWN increases from 239.8 to 278.4 W m^{-2}, approaching the observed 283.0 W m^{-2}. LWP shows consistent enhancement across the hierarchy. At BAR, values rise from 3.8 g m^{-2} (WDM6) to 5.0 (WDM6_IN), 55.7 (WDM6_SP), 103.5 (WDM6_SP_IN), and 178.1 (WDM6_ICE), close to the observed 214.5 g m^{-2} (Table 3). IWP shows a different pattern from LWC: WDM6 produces 38.0 g m^{-2}, exceeding the observed value of 31.5 g m^{-2}, while WDM6_IN maintains a comparable level (33.5 g m^{-2}). The shape-modified configurations reduce IWP substantially (WDM6_SP: 20.8, WDM6_SP_IN: 22.5 g m^{-2}), and WDM6_ICE produces the lowest IWP (10.6 g m^{-2}). This pattern is consistent with the IWC profiles (Fig. 6c, d): nucleation modification alone redistributes ice among hydrometeor categories without reducing total ice content, whereas ice shape modification drives the primary IWP reduction.

https://doi.org/10.5194/egusphere-2026-1486
Preprint. Discussion started: 24 March 2026

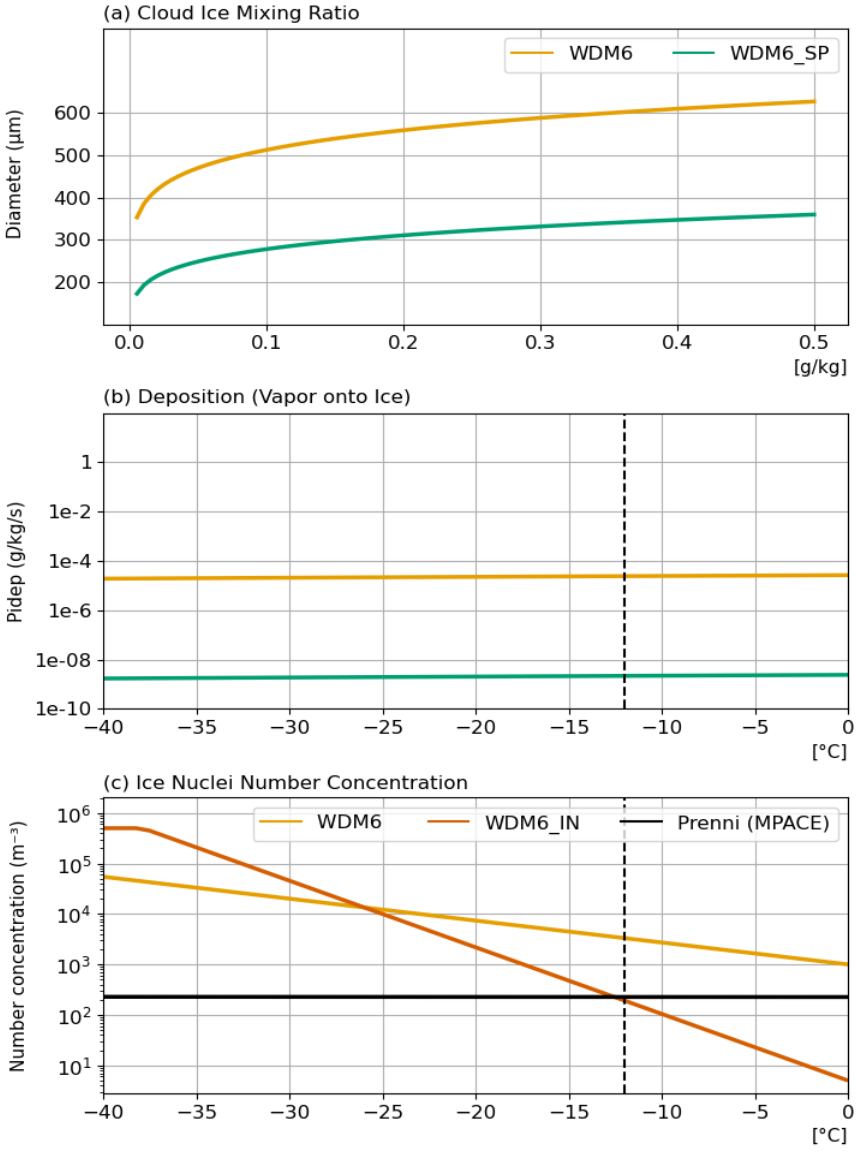

Figure 7: (a) Relationship between cloud ice mixing ratio and diameter in WDM6 (orange) and WDM6_SP (green). (b) Deposition rate of water vapor onto ice (assuming ice mixing ratio of 0.1 g kg^{-1} and supersaturation of 10%) as a function of temperature. (c) INP number concentration (m^{-3}) as a function of temperature. Black line shows M-PACE observations (Prenni et al., 2007); orange and vermillion lines show WDM6 and WDM6_IN parameterizations, respectively. Note that the observational upper limit of 500 L^{-1} (DeMott et al., 2010) corresponds to 5 × 10^{5} m^{-3}. The vertical dashed line marks −12 °C, representing the approximate cloud-top temperature during M-PACE.

https://doi.org/10.5194/egusphere-2026-1486
Preprint. Discussion started: 24 March 2026

The spherical ice assumption reduces particle diameter by approximately 40%. At an ice content of 0.1 g kg^{-1}, diameters decrease from 500 µm in WDM6 to 300 µm in WDM6_SP (Fig. 7a), reducing surface area for vapor deposition.

The size change reduces deposition efficiency (Fig. 7b). At −12 °C, deposition rates decrease from 10^{-4} to 10^{-8} g kg^{-1} s^{-1}, a four-order-of-magnitude reduction. This is consistent with the reduced PIDEP in WDM6_ICE (Fig. 5c).

Ice-nucleating particle (INP) concentration further modulates ice production (Fig. 7c). At the M-PACE cloud-top temperature of approximately −12 °C (Fu et al., 2019), WDM6 produces 3320 m^{-3} INPs, overestimating M-PACE observations (~200 m^{-3}; Prenni et al., 2007) by more than an order of magnitude. WDM6_IN reduces concentrations to 191 m^{-3}, closely matching observations. This represents a 17-fold reduction relative to WDM6. The differences between WDM6_SP_IN and WDM6_ICE (Figs. 3 and 6) indicate that the remaining structural differences in WDM6_ICE produce additional ice reduction beyond the combined effects of shape and nucleation modifications alone.

4 Discussion

4.1 Mechanisms Driving Phase Partitioning Differences

The behaviors of WDM6 and WDM6_ICE reflect a fundamental difference in how available water vapor is partitioned between ice and liquid phases. WDM6 retains the classical Arctic modeling bias of severely underestimating supercooled liquid water (Klein et al., 2009), producing negligible LWP and intermittent cloud coverage because rapid ice growth through the Wegener–Bergeron–Findeisen (WBF) process efficiently drains available liquid water. In WDM6, intense vapor deposition onto bullet-shaped ice particles (PIDEP ~1.6 g kg^{-1} h^{-1}) consumes vapor rapidly, creating subsaturated conditions with respect to water that inhibit liquid maintenance and suppress condensation (PCOND < 0.08 g kg^{-1} h^{-1}).

In WDM6_ICE, the near-complete suppression of PIDEP (reduced to ~0.03 g kg^{-1} h^{-1}, a 98% reduction) redirects the available vapor toward condensation (PCOND > 2.0 g kg^{-1} h^{-1}), sustaining the liquid layer. The dominant vapor consumption pathway shifts from deposition onto cloud ice followed by aggregation into snow to direct snow deposition via PSDEP, which increases threefold. This pathway shift is reflected in the total IWC: while cloud ice is nearly eliminated, snow maintains residual ice content (~0.01 g m^{-3} at BAR), reducing total IWC by approximately 70–80% relative to WDM6 rather than eliminating ice entirely. Although this enhanced liquid water improves radiative and thermal agreement with observations, the substantial reduction in total ice content (IWP of 10.6 g m^{-2} vs. observed 31.5 g m^{-2}) and the shift from a cloud-ice-dominated to a snow-dominated ice budget highlight the challenge of maintaining a balanced mixed-phase state.

The comparison between WDM6_SP_IN and WDM6_ICE demonstrates that structural differences beyond ice shape and nucleation introduce additional ice suppression. Although WDM6_ICE incorporates ice-enhancing mechanisms absent in WDM6_SP_IN (specifically contact freezing active below −2 °C and secondary ice production via the Hallett–Mossop process from −8 to −3 °C), its total ice content remains substantially lower (IWC ~0.01 vs. ~0.03 g m^{-3}; IWP 10.6 vs. 22.5 g m^{-2}). This difference encompasses multiple factors: the prognostic treatment of cloud ice number concentration, the

https://doi.org/10.5194/egusphere-2026-1486
Preprint. Discussion started: 24 March 2026

restricted temperature threshold for vapor deposition nucleation (−8 °C in WDM6_ICE vs. 0 °C in WDM6_SP_IN; see Appendix A3.2), and the additional ice-phase processes themselves. Among these, the prognostic treatment represents the most fundamental structural change. Diagnostic schemes instantaneously recalculate ice number concentration from ice mass at each timestep, so that ice particles are replenished whenever mass recovers through deposition, creating a resilient ice number concentration. In contrast, prognostic treatment tracks cloud ice number concentration through explicit source and sink terms: when particles sublimate completely, they are permanently removed and recovery requires new nucleation events. Under the constrained nucleation and suppressed growth rates shown in Figure 7, this prognostic formulation produces irreversible ice number depletion. Sublimation permanently removes particles from the ice number concentration budget while inadequate nucleation prevents replenishment, progressively driving the system toward cloud ice depletion. The following analysis suggests that the additional ice-enhancing processes in WDM6_ICE are effectively inactive under the present Arctic conditions, supporting the inference that the prognostic treatment is the primary driver of the additional ice suppression.

The limited influence of contact freezing and Hallett–Mossop mechanisms in WDM6_ICE reflects the compound effect of unfavorable environmental conditions and constrained particle growth. The cloud-layer temperatures in the M-PACE case ranged from approximately −15 °C to −10 °C, outside the Hallett–Mossop activation window of −8 °C to −3 °C (Hallett and Mossop, 1974). As noted by Luo et al. (2008), M-PACE cloud temperatures fall outside this range. Additionally, the simulated mean effective ice radius remains near 10–12 μm (Fig. 3f), which is substantially smaller than the particle sizes typically required for efficient riming (>25–50 μm; Pruppacher and Klett, 2010). Specifically, the riming process in WDM6_ICE (Piacw; accretion of cloud water by cloud ice) is parameterized to activate only when the mean-volume diameter of cloud ice exceeds 50 μm (Park and Lim, 2023). Given that the simulated effective ice radius in WDM6_ICE remains at 10–12 μm (corresponding to mean-volume diameters well below 50 μm), this threshold is never satisfied, effectively precluding riming as an ice growth pathway. The spherical shape assumption exacerbates this suppression by limiting depositional growth efficiency, preventing particles from reaching sizes that would satisfy the geometric requirements for these processes. This combination of temperature and size constraints creates an effective constraint on ice multiplication in the present case. These cascading interactions, including constrained nucleation, suppressed deposition, and irreversible number depletion, raise the question of whether this response is specific to Arctic conditions or inherent to the modifications themselves.

4.2 Regime-Dependent Response of Ice Microphysical Modifications

The regime-dependent nature of these responses becomes evident when comparing the present Arctic results with the mid-latitude evaluations of Park and Lim (2023). In their study, the same WDM6_ICE modifications reduced cloud ice mixing ratio through inefficient Pidep and Pinud processes, and the resulting surplus water vapor enhanced liquid water production through condensation (their Figures 8 and 10). Notably, WDM6_ICE simulated higher cloud ice number concentrations despite lower mixing ratios in the mid-latitude cases, indicating that ice particles became more numerous but smaller. The

https://doi.org/10.5194/egusphere-2026-1486
Preprint. Discussion started: 24 March 2026

vapor pathway shift from cloud ice deposition to snow deposition was also evident in their warm-low cases, where enhanced Psdep partially compensated for the reduced cloud ice (their Figure 13). Precipitation skill scores showed mixed results, with notable bias reduction for the cold-low cases but deterioration in some warm-low cases (their Table 3). However, the magnitude and consequences of this pathway diverge between the two regimes. In the mid-latitude ICE-POP cases, hydrometeors extended through deep layers, reaching the 10-km level in warm-low cases (their Figure 11), implying a broader temperature range over which the Cooper curve still permits substantial nucleation, and synoptic-scale forcing continuously supplied moisture. Under these conditions, cloud ice mixing ratio decreased but ice remained present throughout the cloud layer with increased number concentrations, and the total ice budget was moderated rather than fundamentally restructured. In the present Arctic case, cloud-layer temperatures remain within a narrow range (approximately −15 to −10 °C) where nucleation rates under the Cooper curve are inherently limited. Combined with the shallow boundary-layer circulation characteristic of Arctic stratiform systems, which confines moisture supply and nucleation opportunities to a narrow vertical extent unlike the deep tropospheric lifting in mid-latitude cyclonic systems, and the absence of INP recycling, the same modifications produce a more pronounced response: cloud ice is nearly depleted, ice number concentration decreases rather than increases, and the residual ice content is maintained almost entirely through snow deposition (IWP reduced from 38.0 to 10.6 g m^{-2}). While the underlying mechanism is similar to the mid-latitude warm-low cases, the Arctic environment amplifies the response from a moderate adjustment to a fundamental restructuring of the ice budget. This asymmetric response demonstrates that the sensitivity of microphysical parameterizations to environmental conditions is itself regime-dependent: modifications that produce quantitative corrections in one regime can trigger qualitative shifts in cloud ice budget structure in another.

4.3 Radiative Bias Characteristics Across Configurations

The different microphysical configurations produce systematic variations in surface radiative biases (Table 3). WDM6 permits excessive shortwave transmission and insufficient longwave emission, consistent with its sparse cloud coverage and reduced liquid content. WDM6_ICE reproduces LWDOWN values closely matching observations (278.4 W m^{-2}) through the maintenance of persistent liquid-containing clouds, consistent with earlier findings that supercooled liquid water dominates the radiative coupling between clouds and the surface in the Arctic (Cesana et al., 2012). However, the substantial reduction of cloud ice in WDM6_ICE, with total ice content maintained primarily through snow rather than through a realistic distribution of ice habits (IWP of 10.6 g m^{-2} vs. observed 31.5 g m^{-2}), raises questions about whether this radiative agreement is achieved for physically consistent reasons.The sensitivity experiments reveal a non-linear relationship between LWP and surface temperature. Configurations with intermediate LWP (WDM6_SP, WDM6_SP_IN) produce the warmest simulated surface temperatures (−5.4 °C) despite having smaller LWP than WDM6_ICE (Table 3). This behavior is consistent with the longwave opacity threshold identified by Shupe and Intrieri (2004): once LWP exceeds approximately 30 g m^{-2}, clouds become effectively opaque to longwave radiation and LWDOWN is primarily governed by cloud base

https://doi.org/10.5194/egusphere-2026-1486
Preprint. Discussion started: 24 March 2026

temperature and height rather than by LWP magnitude. Above this threshold, further LWP increases primarily enhance cloud optical depth and reduce shortwave transmission, partially offsetting the longwave warming effect. The higher cloud fractions in these configurations (Fig. S2) further contribute to the shortwave differences. This compensation indicates that, from a surface energy perspective, configurations with intermediate LWP can produce comparable or smaller temperature biases compared with configurations that maximize liquid water.

4.4 Structural Constraints and Future Directions

Despite improved agreement with observed surface radiative forcing, all configurations underestimate total water path (TWP = LWP + IWP; 189 g m^{-2} versus 246 g m^{-2} observed at BAR). This underestimation reflects contributions from multiple sources. The water vapor profiles show that ERA5 boundary conditions are drier than observations within the cloud layer (Fig. S3), providing an insufficient moisture supply for all configurations. Beyond this initial data constraint, microphysical processes further limit condensate production. WDM6 retains more moisture in the lower boundary layer than WDM6_ICE yet does not maintain liquid water, confirming that the ice-dominated behavior in WDM6 results from excessive vapor consumption by ice deposition rather than from insufficient moisture supply. The absence of INP recycling may also contribute: when ice particles sublimate, the released nuclei are not returned to the available INP population, permanently reducing the capacity for subsequent ice formation (Fu et al., 2019). Although WDM6_IN reproduces observed INP concentrations (Fig. 7c), total IWP remains comparable to WDM6 (33.5 vs. 38.0 g m^{-2}) because the Cooper curve redistributes ice from cloud ice to snow rather than reducing total ice content. This indicates that correcting INP number alone is insufficient to improve Arctic ice representation when the ice growth pathway remains unconstrained. To assess the robustness of these results to boundary-layer parameterization, additional simulations were performed using the Shin and Hong (2015) PBL scheme. The overall LWC sensitivity hierarchy and the dominant role of ice shape modification are consistent across both PBL schemes (Fig. S4). The magnitude of IWC reduction in WDM6_ICE varies between PBL schemes (IWC peak of ~0.01 g m^{-3} with YSU vs. ~0.03 g m^{-3} with Shin and Hong, 2015), indicating some interaction between prognostic ice treatment and boundary-layer mixing, while the qualitative regime-dependent responses remain robust.The excessive droplet production in WDM6_ICE (~890 cm^{-3}) introduces additional feedback loops that reinforce ice suppression. In WDM6_ICE, immersion freezing following the Bigg (1953) parameterization contributes negligibly to ice production. Although the droplet number concentration is high (~890 cm^{-3}), the small droplet sizes (effective radii 5–6 μm) reduce the per-droplet freezing probability, and the net immersion freezing rate remains insufficient to sustain ice formation. The prescribed CCN floor of 100 cm^{-3} (Table 1) amplifies this feedback asymmetrically: in WDM6, strong vapor deposition prevents sustained water supersaturation so the CCN reservoir remains largely inactive (droplet concentrations reach only ~15–23 cm^{-3}), whereas in WDM6_ICE the suppressed PIDEP allows sustained supersaturation and repeated CCN activation (Fig. 5a). Since Arctic CCN concentrations are generally well below 100 cm^{-3} (Jung et al., 2018; Mauritsen et al., 2011), the enforced minimum maintains an unrealistically large CCN source that sustains excessive droplet production. Systematic investigation of CCN sensitivity constitutes a separate research question beyond the scope of the present study. More

https://doi.org/10.5194/egusphere-2026-1486
Preprint. Discussion started: 24 March 2026

fundamentally, the Bigg parameterization treats immersion freezing as a purely stochastic process without considering aerosol composition. Frameworks such as de Boer et al. (2010), which couple ice nucleation to insoluble material within droplets, or Ong et al. (2024), which incorporate cloud ice shape dependence, represent nucleation pathways structurally absent from WDM6_ICE and suggest that aerosol-aware ice nucleation parameterizations are a priority for Arctic MPC simulation.

As discussed in Section 4.1, the simulated ice particles in WDM6_ICE do not reach the threshold sizes required for efficient riming and secondary ice activation. Fu et al. (2019) identified droplet shattering during heterogeneous freezing as an additional secondary ice mechanism for the same M-PACE case, but this process also depends on the presence of rimed particles. The spherical ice assumption creates a self-reinforcing constraint: by limiting depositional growth, it prevents cloud ice particles from reaching the sizes necessary for riming and ice multiplication, confining the ice budget to a snow-dominated state where cloud ice is nearly absent. Consistent with the regime-dependent response discussed in Section 4.2, this constraint acts differently across environments, moderating excessive ice production in mid-latitude systems (Park and Lim, 2023) while producing a fundamental restructuring of the ice budget under the narrow Arctic temperature range. These findings suggest that representing regime-consistent ice microphysics may benefit from shape-dependent growth formulations that allow deposition efficiency to vary with particle size and environmental conditions.

5 Conclusion

This study evaluated the behavior of the WDM6 and WDM6_ICE microphysics schemes under Arctic mixed-phase cloud conditions using the M-PACE case (9–10 October 2004), with sensitivity experiments isolating the effects of ice shape and nucleation modifications.

The two schemes produce opposing biases: WDM6 severely underestimates liquid water due to excessive ice deposition, while WDM6_ICE substantially suppresses cloud ice and shifts the ice budget to a snow-dominated state, maintaining persistent liquid water but with unrealistically high droplet concentrations. The sensitivity decomposition shows that ice shape modification is the dominant factor, reducing vapor deposition onto cloud ice (PIDEP) by approximately 98% and total IWC by 60–80%. Nucleation modification alone (WDM6_IN) does not reduce total ice content but instead redistributes ice from the cloud ice to the snow category, indicating that correcting INP number without constraining ice growth pathways is insufficient for improving Arctic ice representation. The comparison between WDM6_SP_IN and WDM6_ICE indicates that the remaining structural differences, primarily the prognostic ice number treatment, produce additional cloud ice suppression, as irreversible particle loss through sublimation is not compensated by sufficient nucleation under Arctic conditions. While Park and Lim (2023) showed that the same WDM6_ICE modifications reduced cloud ice mixing ratio but maintained cloud ice throughout the cloud layer in mid-latitude cases, the present results show a more pronounced response under Arctic conditions, with cloud ice nearly depleted and ice number concentration decreased rather than increased, suggesting that the response to these modifications is regime-dependent.

https://doi.org/10.5194/egusphere-2026-1486
Preprint. Discussion started: 24 March 2026

Surface energy analysis reveals that configurations with intermediate liquid water path produce surface temperature biases comparable to or smaller than the configuration maximizing liquid water, indicating that balanced phase partitioning is more relevant than liquid water maximization for radiative bias reduction.

These results highlight several structural characteristics of the current WDM6_ICE framework that constrain its Arctic application: the absence of INP recycling, the CCN floor that sustains unrealistic droplet production under suppressed ice conditions, the lack of aerosol-aware immersion freezing, and the fixed spherical ice shape that prevents cloud ice particles from reaching sizes necessary for secondary ice production. These constraints suggest that improving Arctic MPC representation in bulk microphysics schemes may benefit from shape-dependent ice growth formulations and closer coupling between aerosol properties and ice nucleation, though the effectiveness of such approaches remains to be tested.

The prognostic treatment of cloud ice number concentration in WDM6_ICE represents a physically meaningful advancement over the diagnostic approach, as demonstrated by its improved performance in mid-latitude environments (Park and Lim, 2023). Building on this foundation, future development toward Arctic application may benefit from incorporating mechanisms such as INP recycling (Fu et al., 2019), shape-dependent ice growth formulations (e.g., Morrison and Milbrandt, 2015), and aerosol-aware ice nucleation (e.g., de Boer et al., 2010; Ong et al., 2024). Such extensions would help bridge the gap between mid-latitude and Arctic performance, contributing to more physically consistent scheme behavior across diverse climate regimes.

https://doi.org/10.5194/egusphere-2026-1486
Preprint. Discussion started: 24 March 2026

Appendices

This appendix focuses on the parameterizations most relevant to the present sensitivity experiments.

A1. WDM6 parameterizations

The baseline WDM6 scheme uses temperature-based ice nucleation and ice-mass-dependent cloud ice number concentration. Ice particles are assumed to have bullet shapes with coefficients from Heymsfield & Iaquinta (2000).

A1.1. Ice-nucleating particle (INP) number concentration (Diagnostic)

$$N_{I0}[m^{-3}] = 10^3 \times \exp[0.1(T_0 - T)], \quad \text{(A1)}$$

(Note: INP number concentration presented as N_{I0} in Hong et al. (2004), N_{IND} in Park & Lim (2023))

A1.2. Cloud ice number concentration (Diagnostic)

$$N_I[m^{-3}] = 5.38 \times 10^7 (\rho q_I)^{0.75}, \quad \text{(A2)}$$

1. N_I has no memory of previous timesteps
2. Any change in q_I immediately adjusts N_I
3. Ice number population recovers instantly when ice mass increases
4. Sink terms (sublimation, sedimentation) affect q_I, which then diagnostically adjusts N_I. This formulation creates tight coupling between ice mass and number, preventing independent evolution of particle size distributions.

A1.3. Ice particle properties (Single bullet Shape)

A1.3.1. Mass-diameter relationship

$$M_I[kg] = \left(\frac{1}{11.9}\right)^{2.0} D_I^{2.0} \left(\frac{\rho_0}{\rho_a}\right)^{0.5}, \quad \text{(A3)}$$

A1.3.2. Fall velocity-diameter relationship

$$V_I[ms^{-1}] = 1.49 \times 10^4 D_I^{1.31}, \quad \text{(A4)}$$

A2. Sensitivity Experiment Modifications

A2.1. Spherical ice shape

Based on Brown & Francis (1995) and Korolev & Isaac (2003), ice particles are assumed spherical with bulk density (ρ_I).

A2.1.1. Mass-diameter relationship

$$M_I[kg] = \left(\frac{\pi \rho_I}{6}\right) D_I^{3.0}, \ (\rho_I[kgm^{-3}] = 500), \quad \text{(A5)}$$

A2.1.2. Fall velocity-diameter relationship

https://doi.org/10.5194/egusphere-2026-1486
Preprint. Discussion started: 24 March 2026

$$V_I[ms^{-1}] = 2710 \times D_I^{1.0} \left(\frac{\rho_0}{\rho_a}\right)^{0.5}, \quad \text{(A6)}$$

480

A2.2. Modified Ice Nucleation

Based on Cooper (1986) temperature-dependent nucleation with observational upper limit (DeMott et al., 2010), active at T < 0 °C. Vapor depositional/condensation freezing.

$$N_{I0}\ [m^{-3}s^{-1}] = 5 \times \exp[0.304(T_0 - T)]\,,\ (max\ 500\ L^{-1}), \quad \text{(A7)}$$

485

A3. WDM6_ICE Parameterizations

WDM6_ICE combines spherical ice shape (Section A2.1) with prognostic cloud ice number concentration treatment and modified nucleation implementation. Although WDM6_ICE includes additional processes such as contact freezing, Hallett-Mossop multiplication, and graupel category (see Park & Lim, 2023 for complete detail), this appendix focuses on the
490 parameterizations most relevant to the present sensitivity experiments.

A3.1 Prognostic Cloud Ice Number Concentration

WDM6_ICE treats cloud ice number concentration (N_I) as a prognostic variable. The ice size distribution is represented by a gamma function:

495 $$N_I(D_I)[m^{-4}] = N_{0I}^{\mu_I} \exp\{-(\lambda_I D_I)\}, \quad \text{(A8)}$$

Where the intercept (N_{0I}) and slope (λ_I) are diagnosed from prognostic N_I and ice mixing ratio (q_I) through mass-diameter relationships (Section A2.1). The shape parameter (μ_I) is prescribed. The prognostic N_I evolves through nucleation (vapor deposition, contact freezing, immersion freezing), ice multiplication (Hallett-Mossop), sublimation, melting, aggregation, and sedimentation.

500 This prognostic treatment fundamentally differs from the diagnostic approach (Section A1.2) in how N_I responds to changes in ice mass:

- Diagnostic (WDM6): N_I recalculated every timestep → if qi recovers through deposition, N_I instantly recovers

- Prognostic (WDM6_ICE): N_I evolves through explicit source/sink terms → if particles sublimate or sediment, they are permanently removed from N_I; recovery requires new nucleation events This decoupling creates potential for irreversible N_I
505 depletion when: (1) nucleation is constrained (e.g., WDM6_IN: 191 vs 3320 m⁻³), limiting the source term, and (2) particle growth is suppressed (e.g., WDM6_SP: spherical ice reducing deposition), increasing relative importance of sink terms (sublimation, sedimentation).

A3.2. Modified Ice Nucleation Implementation

https://doi.org/10.5194/egusphere-2026-1486
Preprint. Discussion started: 24 March 2026

INP number concentration (N_{IND}) remains diagnostic following the Cooper curve (Section A2.2), but vapor depositional/condensational freezing (Ninud) is implemented differently from WDM6_IN and WDM6_SP_IN. The key difference is the temperature threshold: WDM6_IN and WDM6_SP_IN activate Ninud at T < 0°C, while WDM6_ICE restricts activation to T < -8°C.

The prognostic formulation calculates cloud ice number and mass increments as:

$$Ninud[m^{-3}s^{-1}] = \frac{N_{IND}-N_I}{\Delta t},\ (when\ N_{IND} > N_I), \quad \text{(A9)}$$

$$Pinud[kgkg^{-1}s^{-1}] = Ninud\ \times \frac{M_{IND}}{\rho_a}, \quad \text{(A10)}$$

Where M_{IND} is the initial mass of the nucleated cloud ice, calculated as $M_{IND} = \frac{4\pi\rho_I}{3} \times (\mathrm{R}_{IND})^3$ with R_{IND}(10 μm) being initial radius of the nucleated cloud ice. This approach directly updates prognostic N_I, which then affects size distribution parameters and subsequent microphysical processes.

This differs from WDM6_IN (Section A.2.2), which converts N_{IND} directly to ice mass (Pigen) and diagnoses N_I from q_I at each time step. Between 0°C and -8°C, WDM6_ICE does not nucleate new cloud ice through vapor deposition, but existing ice particles continue to grow via vapor deposition (Pidep, active at T < 0°C), immersion freezing, and contact freezing (T < -2°C).

Data Availability

The WRF model version 4.3.1 is described in Skamarock et al. (2021) and available at https://doi.org/10.5065/1dfh-6p97.

Initial and boundary conditions were obtained from the ERA5 reanalysis: ERA5 pressure level data (https://doi.org/10.24381/cds.bd0915c6, Hersbach et al., 2023a) and ERA5 single level data (https://doi.org/10.24381/cds.adbb2d47, Hersbach et al., 2023b).

Observation data can be accessed through the Atmospheric Radiation Measurement (ARM) User Facility. Aircraft in-situ microphysics data from the M-PACE campaign (McFarquhar, 2007) are available from the ARM Data Center at https://adc.arm.gov/discovery/results/iopShortName::nsa2004arcticcld. Access requires free registration at https://adc.arm.gov. Surface station data are available from the ARM Data Center: ARMBEATM (https://doi.org/10.5439/1333748, Chen and Xie, 2001), ACRED (https://doi.org/10.5439/1995948, Xie, 1999), MWRRET (https://doi.org/10.5439/1027369, Zhang, 2001), QCRAD (https://doi.org/10.5439/1027372, Zhang, 1998), and radiosonde (https://doi.org/10.5439/1595321, Keeler et al., 2002).

The model code for WDM6_ICE is publicly available at Zenodo (https://doi.org/10.5281/zenodo.7395819, Park, 2023). The model codes for WDM6_SP and WDM6_SP_IN experiments, along with figure generation scripts, are archived at Zenodo (Sung, 2026; https://doi.org/10.5281/zenodo.19049015). During peer review, access is provided via a private link (https://zenodo.org/records/19049015?preview=1&token=eyJhbGciOiJIUzUxMiJ9.eyJpZCI6IjRmMTQzODI2LTE4OTktNDZhOC05MWM4LWNhNDQzODkyNjQzZCIsImRhdGEiOnt9LCJyYW5kb20iOiJiMGViODE1NjAyODFmMjExODIzY

https://doi.org/10.5194/egusphere-2026-1486
Preprint. Discussion started: 24 March 2026

mQwNGQ1NDMzMTIwZiJ9.Q_yDp99cAPfFwk3VPlSB6LbvF8tBySuiD89tRWTu_BoGE1qpA1Wwv1pQ5RuHFuBO53MZ60H745Hj-5czDKukZA). Model outputs are available upon request (Hyun-Joon Sung via sereno2359@gmail.com).

Supplement link

The link to the supplement will be included by Copernicus,

Author contributions

Hyun-Joon Sung: Conceptualization, Formal analysis, Visualization, Writing – original draft, **Kyo-Sun Sunny Lim:** Validation, Writing – review & editing, **Song-You Hong:** Validation, Writing – review & editing, **JiHoon Shin:** Validation, **Baek-Min Kim:** Supervision, Funding acquisition, **Ji-Hun Choi:** Visualization

Competing interests

The contact author has declared that none of the authors has any competing interests.

Disclaimer

Copernicus Publications adds a standard disclaimer: “Copernicus Publications remains neutral with regard to jurisdictional claims made in the text, published maps, institutional affiliations, or any other geographical representation in this paper. While Copernicus Publications makes every effort to include appropriate place names, the final responsibility lies with the authors. Views expressed in the text are those of the authors and do not necessarily reflect the views of the publisher.”

Acknowledgements

https://doi.org/10.5194/egusphere-2026-1486
Preprint. Discussion started: 24 March 2026

Financial support

This research was supported by the Korea-Arctic Ocean Warming and Response of Ecosystem, KOPRI) and by the Korea Polar Research Institute (KOPRI) grant funded by the Ministry of Oceans and Fisheries (KOPRI (grant no. PE25010)).

Review statement

The review statement will be added by Copernicus Publications listing the handling editor as well as all contributing referees according to their status anonymous or identified.

References

Bigg, E.K., 1953. The Supercooling of Water. Proc. Phys. Soc. Sect. B 66, 688. https://doi.org/10.1088/0370-1301/66/8/309

Brown, P.R.A., Francis, P.N., 1995. Improved Measurements of the Ice Water Content in Cirrus Using a Total-Water Probe. J. Atmos. Ocean. Technol. 12, 410–414. https://doi.org/10.1175/1520-0426(1995)012<0410:IMOTIW>2.0.CO;2

Cesana, G., Kay, J.E., Chepfer, H., English, J.M., De Boer, G., 2012. Ubiquitous low-level liquid-containing Arctic clouds: New observations and climate model constraints from CALIPSO-GOCCP. Geophys. Res. Lett. 39. https://doi.org/10.1029/2012GL053385

Chen, F., Dudhia, J., 2001. Coupling and advanced land surface-hydrology model with the Penn State-NCAR MM5 modeling system. Part I: Model implementation and sensitivity. Mon. Weather Rev. 129, 569–585. https://doi.org/10.1175/1520-0493(2001)129<0569:CAALSH>2.0.CO;2

Chen, X., Xie, S. ARM Best Estimate Data Products (ARMBEATM), 2001-01-01 to 2023-12-31, North Slope Alaska (NSA), Central Facility, Barrow AK (C1). Atmospheric Radiation Measurement (ARM) User Facility. https://doi.org/10.5439/1333748

Comin, A.N., Schumacher, V., Justino, F., 2018. Impact of different microphysical parameterizations on extreme snowfall events in the Southern Andes. Weather Clim. Extrem. 21, 65–75. https://doi.org/10.1016/J.WACE.2018.07.001

Cooper, W.A., 1986. Ice Initiation in Natural Clouds. Meteorol. Monogr. 21, 29–32. https://doi.org/10.1175/0065-9401-21.43.29

Cotton, W.R., Tripoli, G.J., Rauber, R.M., Mulvihill, E.A., 1986. Numerical Simulation of the Effects of Varying Ice Crystal Nucleation Rates and Aggregation Processes on Orographic Snowfall. J. Appl. Meteorol. Climatol. 25, 1658–1680. https://doi.org/10.1175/1520-0450(1986)025<1658:NSOTEO>2.0.CO;2

de Boer, G., Hashino, T., Tripoli, G.J., 2010. Ice nucleation through immersion freezing in mixed-phase stratiform clouds: Theory and numerical simulations. Atmos. Res. 96, 315–324. https://doi.org/10.1016/j.atmosres.2009.09.012

DeMott, P.J., Prenni, A.J., Liu, X., Kreidenweis, S.M., Petters, M.D., Twohy, C.H., Richardson, M.S., Eidhammer, T., Rogers, D.C., 2010. Predicting global atmospheric ice nuclei distributions and their impacts on climate. Proc. Natl.

https://doi.org/10.5194/egusphere-2026-1486
Preprint. Discussion started: 24 March 2026

Acad. Sci. U. S. A. 107, 11217–11222. https://doi.org/10.1073/PNAS.0910818107/SUPPL_FILE/PNAS.0910818107_SI.PDF

Fridlind, A.M., Ackerman, A.S., Chaboureau, J.P., Fan, J., Grabowski, W.W., Hill, A.A., Jones, T.R., Khaiyer, M.M., Liu, G., Minnis, P., Morrison, H., Nguyen, L., Park, S., Petch, J.C., Pinty, J.P., Schumacher, C., Shipway, B.J., Varble, A.C., Wu, X., Xie, S., Zhang, M., 2012. A comparison of TWP-ICE observational data with cloud-resolving model results. J. Geophys. Res. Atmos. 117. https://doi.org/10.1029/2011JD016595

Fridlind, A.M., Ackerman, A.S., McFarquhar, G., Zhang, G., Poellot, M.R., DeMott, P.J., Prenni, A.J., Heymsfield, A.J., 2007. Ice properties of single-layer stratocumulus during the Mixed-Phase Arctic Cloud Experiment: 2. Model results. J. Geophys. Res. Atmos. 112, 24202. https://doi.org/10.1029/2007JD008646;REQUESTEDJOURNAL:JOURNAL:21562202D;PAGE:STRING:ARTICLE/CHAPTER

Fu, S., Deng, X., Shupe, M.D., Xue, H., 2019. A modelling study of the continuous ice formation in an autumnal Arctic mixed-phase cloud case. Atmos. Res. 228, 77–85. https://doi.org/10.1016/J.ATMOSRES.2019.05.021

Hallett, J., Mossop, S.C., 1974. Production of secondary ice particles during the riming process. Nature 249, 26–28. https://doi.org/10.1038/249026A0;KWRD=SCIENCE

Hersbach, H., Bell, B., Berrisford, P., Hirahara, S., Horányi, A., Muñoz-Sabater, J., Nicolas, J., Peubey, C., Radu, R., Schepers, D., Simmons, A., Soci, C., Abdalla, S., Abellan, X., Balsamo, G., Bechtold, P., Biavati, G., Bidlot, J., Bonavita, M., De Chiara, G., Dahlgren, P., Dee, D., Diamantakis, M., Dragani, R., Flemming, J., Forbes, R., Fuentes, M., Geer, A., Haimberger, L., Healy, S., Hogan, R.J., Hólm, E., Janisková, M., Keeley, S., Laloyaux, P., Lopez, P., Lupu, C., Radnoti, G., de Rosnay, P., Rozum, I., Vamborg, F., Villaume, S., Thépaut, J.N., 2020. The ERA5 global reanalysis. Q. J. R. Meteorol. Soc. 146, 1999–2049. https://doi.org/10.1002/QJ.3803

Hersbach, H., Bell, B., Berrisford, P., Biavati, G., Horányi, A., Muñoz Sabater, J., Nicolas, J., Peubey, C., Radu, R., Rozum, I., Schepers, D., Simmons, A., Soci, C., Dee, D., Thépaut, J-N. (2023): ERA5 hourly data on pressure levels from 1940 to present. Copernicus Climate Change Service (C3S) Climate Data Store (CDS), DOI: 10.24381/cds.bd0915c6 (Accessed on 18-03-2026)

Hersbach, H., Bell, B., Berrisford, P., Biavati, G., Horányi, A., Muñoz Sabater, J., Nicolas, J., Peubey, C., Radu, R., Rozum, I., Schepers, D., Simmons, A., Soci, C., Dee, D., Thépaut, J-N. (2023): ERA5 hourly data on single levels from 1940 to present. Copernicus Climate Change Service (C3S) Climate Data Store (CDS), DOI: 10.24381/cds.adbb2d47 (Accessed on 18-03-2026)

Heymsfield, A.J., Iaquinta, J., 2000. Cirrus Crystal Terminal Velocities. J. Atmos. Sci. 57, 916–938. https://doi.org/10.1175/1520-0469(2000)057<0916:CCTV>2.0.CO;2

Hong, S.-Y., Dudhia, J., Chen, S.-H., 2004. A Revised Approach to Ice Microphysical Processes for the Bulk Parameterization of Clouds and Precipitation. Mon. Weather Rev. 132, 103–120. https://doi.org/10.1175/1520-0493(2004)132<0103:ARATIM>2.0.CO;2

https://doi.org/10.5194/egusphere-2026-1486
Preprint. Discussion started: 24 March 2026

Hong, S.Y., Noh, Y., Dudhia, J., 2006. A New Vertical Diffusion Package with an Explicit Treatment of Entrainment Processes. Mon. Weather Rev. 134, 2318–2341. https://doi.org/10.1175/MWR3199.1

Iacono, M.J., Delamere, J.S., Mlawer, E.J., Shephard, M.W., Clough, S.A., Collins, W.D., 2008. Radiative forcing by long-lived greenhouse gases: Calculations with the AER radiative transfer models. J. Geophys. Res. Atmos. 113. https://doi.org/10.1029/2008JD009944

Jiménez, P.A., Dudhia, J., González-Rouco, J.F., Navarro, J., Montávez, J.P., García-Bustamante, E., 2012. A Revised Scheme for the WRF Surface Layer Formulation. Mon. Weather Rev. 140, 898–918. https://doi.org/10.1175/MWR-D-11-00056.1

Jung, C.H., Yoon, Y.J., Kang, H.J., Gim, Y., Lee, B.Y., Ström, J., Krejci, R., Tunved, P., 2018. The seasonal characteristics of cloud condensation nuclei (CCN) in the arctic lower troposphere. Tellus, Ser. B Chem. Phys. Meteorol. 70, 1–13. https://doi.org/10.1080/16000889.2018.1513291

Keeler, E., Burk, K., & Kyrouac, J. Balloon-Borne Sounding System (SONDEWNPN), 2002-04-28 to 2026-03-18, North Slope Alaska (NSA), Central Facility, Barrow AK (C1). Atmospheric Radiation Measurement (ARM) User Facility. https://doi.org/10.5439/1595321

Klein, S.A., McCoy, R.B., Morrison, H., Ackerman, A.S., Avramov, A., de Boer, G., Chen, M., Cole, J.N.S., del Genio, A.D., Falk, M., Foster, M.J., Fridlind, A., Golaz, J.C., Hashino, T., Harrington, J.Y., Hoose, C., Khairoutdinov, M.F., Larson, V.E., Liu, X., Luo, Y., McFarquhar, G.M., Menon, S., Neggers, R.A.J., Park, S., Poellot, M.R., Schmidt, J.M., Sednev, I., Shipway, B.J., Shupe, M.D., Spangenberg, D.A., Sud, Y.C., Turner, D.D., Veron, D.E., von Salzen, K., Walker, G.K., Wang, Z., Wolf, A.B., Xie, S., Xu, K.M., Yang, F., Zhang, G., 2009. Intercomparison of model simulations of mixed-phase clouds observed during the ARM Mixed-Phase Arctic Cloud Experiment. I: Single-layer cloud. Q. J. R. Meteorol. Soc. 135, 979–1002. https://doi.org/10.1002/QJ.416;WGROUP:STRING:PUBLICATION

Korolev, A., Isaac, G., 2003. Roundness and Aspect Ratio of Particles in Ice Clouds. J. Atmos. Sci. 60, 1795–1808. https://doi.org/10.1175/1520-0469(2003)060<1795:RAAROP>2.0.CO;2

Lim, K.S.S., Hong, S.Y., 2010. Development of an Effective Double-Moment Cloud Microphysics Scheme with Prognostic Cloud Condensation Nuclei (CCN) for Weather and Climate Models. Mon. Weather Rev. 138, 1587–1612. https://doi.org/10.1175/2009MWR2968.1

Luo, Y., Xu, K.M., Morrison, H., McFarquhar, G., 2008. Arctic Mixed-Phase Clouds Simulated by a Cloud-Resolving Model: Comparison with ARM Observations and Sensitivity to Microphysics Parameterizations. J. Atmos. Sci. 65, 1285–1303. https://doi.org/10.1175/2007JAS2467.1

Mauritsen, T., Sedlar, J., TjernstrÃm, M., Leck, C., Martin, M., Shupe, M., Sjogren, S., Sierau, B., Persson, P.O.G., Brooks, I.M., Swietlicki, E., 2011. An Arctic CCN-limited cloud-aerosol regime. Atmos. Chem. Phys. 11, 165–173. https://doi.org/10.5194/acp-11-165-2011

https://doi.org/10.5194/egusphere-2026-1486
Preprint. Discussion started: 24 March 2026

McFarquhar, G.M., Zhang, G., Poellot, M.R., Kok, G.L., McCoy, R., Tooman, T., Fridlind, A., Heymsfield, A.J., 2007. Ice properties of single-layer stratocumulus during the Mixed-Phase Arctic Cloud Experiment: 1. Observations. J. Geophys. Res. Atmos. 112. https://doi.org/10.1029/2007JD008633

McMillen, J.D., James Steenburgh, W., 2015. Impact of Microphysics Parameterizations on Simulations of the 27 October 2010 Great Salt Lake–Effect Snowstorm. Weather Forecast. 30, 136–152. https://doi.org/10.1175/WAF-D-14-00060.1

Morrison, H., Curry, J.A., Khvorostyanov, V.I., Morrison, H., Curry, J.A., Khvorostyanov, V.I., 2005. A New Double-Moment Microphysics Parameterization for Application in Cloud and Climate Models. Part I: Description. J. Atmos. Sci. 62, 1665–1677. https://doi.org/10.1175/JAS3446.1

Morrison, H., De Boer, G., Feingold, G., Harrington, J., Shupe, M.D., Sulia, K., 2012. Resilience of persistent Arctic mixed-phase clouds. Nat. Geosci. https://doi.org/10.1038/ngeo1332

Morrison, H., McCoy, R.B., Klein, S.A., Xie, S., Luo, Y., Avramov, A., Chen, M., Cole, J.N.S., Falk, M., Foster, M.J., del Genio, A.D., Harrington, J.Y., Hoose, C., Khairoutdinov, M.F., Larson, V.E., Liu, X., McFarquhar, G.M., Poellot, M.R., von Salzen, K., Shipway, B.J., Shupe, M.D., Sud, Y.C., Turner, D.D., Veron, D.E., Walker, G.K., Wang, Z., Wolf, A.B., Xu, K.M., Yang, F., Zhang, G., 2009. Intercomparison of model simulations of mixed-phase clouds observed during the ARM Mixed-Phase Arctic Cloud Experiment. II: Multilayer cloud. Q. J. R. Meteorol. Soc. 135, 1003–1019. https://doi.org/10.1002/QJ.415;WGROUP:STRING:PUBLICATION

Morrison, H., Milbrandt, J.A., 2015. Parameterization of Cloud Microphysics Based on the Prediction of Bulk Ice Particle Properties. Part I: Scheme Description and Idealized Tests. J. Atmos. Sci. 72, 287–311. https://doi.org/10.1175/JAS-D-14-0065.1

Morrison, H., Pinto, J.O., 2006. Intercomparison of Bulk Cloud Microphysics Schemes in Mesoscale Simulations of Springtime Arctic Mixed-Phase Stratiform Clouds. Mon. Weather Rev. 134, 1880–1900. https://doi.org/10.1175/MWR3154.1

Morrison, H., van Lier-Walqui, M., Fridlind, A.M., Grabowski, W.W., Harrington, J.Y., Hoose, C., Korolev, A., Kumjian, M.R., Milbrandt, J.A., Pawlowska, H., Posselt, D.J., Prat, O.P., Reimel, K.J., Shima, S.I., van Diedenhoven, B., Xue, L., 2020. Confronting the Challenge of Modeling Cloud and Precipitation Microphysics. J. Adv. Model. Earth Syst. 12. https://doi.org/10.1029/2019MS001689

Nam, J., Cho, Y., Lim, K.S., Jun, S.Y., Kim, J.H., Park, S.J., Kim, S.W., 2024. Evaluation of Four Cloud Microphysical Schemes Simulating Arctic Low-Level Clouds Observed During the ACLOUD Experiment. Asia-Pacific J. Atmos. Sci. 60, 727–740. https://doi.org/10.1007/S13143-024-00378-0/METRICS

Ong, C.R.U.I., Koike, M., Hashino, T., Miura, H., 2024. Responses of Simulated Arctic Mixed-Phase Clouds to Parameterized Ice Particle Shape. J. Atmos. Sci. 81, 125–152. https://doi.org/10.1175/JAS-D-23-0015.1

Park, S.Y., Lim, K.S.S., 2023. Implementation of Prognostic Cloud Ice Number Concentrations for the Weather Research and Forecasting (WRF) Double-Moment 6-Class (WDM6) Microphysics Scheme. J. Adv. Model. Earth Syst. 15, e2022MS003009. https://doi.org/10.1029/2022MS003009

https://doi.org/10.5194/egusphere-2026-1486
Preprint. Discussion started: 24 March 2026

Park, S.Y., 2023. Code for JAMES publication - Implementation of prognostic cloud ice number concentrations for the Weather Research and Forecasting (WRF) Double-Moment 6-class (WDM6) microphysics scheme. https://doi.org/10.5281/zenodo.7395819

Possner, A., Pfannkuch, K., Ramadoss, V., 2024. Cloud-Resolving ICON Simulations of Secondary Ice Production in Arctic Mixed-Phase Stratocumuli Observed during M-PACE. J. Atmos. Sci. 81, 417–434. https://doi.org/10.1175/JAS-D-23-0069.1

Prenni, A.J., Harrington, J.Y., Tjernström, M., DeMott, P.J., Avramov, A., Long, C.N., Kreidenweis, S.M., Olsson, P.Q., Verlinde, J., 2007. Can Ice-Nucleating Aerosols Affect Arctic Seasonal Climate? Bull. Am. Meteorol. Soc. 88, 541–550. https://doi.org/10.1175/BAMS-88-4-541

Pruppacher, H.R., Klett, J.D., 2010. Microphysics of Clouds and Precipitation. Atmospheric and Oceanographic Sciences Library 18. https://doi.org/10.1007/978-0-306-48100-0

Shin, H.H., Hong, S.Y., 2015. Representation of the Subgrid-Scale Turbulent Transport in Convective Boundary Layers at Gray-Zone Resolutions. Mon. Weather Rev. 143, 250–271. https://doi.org/10.1175/MWR-D-14-00116.1

Shupe, M.D., Daniel, J.S., de Boer, G., Eloranta, E.W., Kollias, P., Long, C.N., Luke, E.P., Turner, D.D., Verlinde, J., 2008. A Focus On Mixed-Phase Clouds: The Status of Ground-Based Observational Methods. Bull. Am. Meteorol. Soc. 89, 1549–1562. https://doi.org/10.1175/2008BAMS2378.1

Shupe, M.D., Intrieri, J.M., 2004. Cloud Radiative Forcing of the Arctic Surface: The Influence of Cloud Properties, Surface Albedo, and Solar Zenith Angle. J. Clim. 17, 616–628. https://doi.org/https://doi.org/10.1175/1520-0442(2004)017<0616:CRFOTA>2.0.CO;2

Skamarock et al., 2021. A Description of the Advanced Research WRF Model Version 4.3 | OpenSky. https://doi.org/https://doi.org/10.5065/1dfh-6p97

Solomon, A., Morrison, H., Persson, O., Shupe, M.D., Bao, J.W., 2009. Investigation of microphysical parameterizations of snow and ice in arctic clouds during M-PACE through model observation comparisons. Mon. Weather Rev. 137, 3110–3128. https://doi.org/10.1175/2009MWR2688.1

Thompson, G., Field, P.R., Rasmussen, R.M., Hall, W.D., Thompson, G., Field, P.R., Rasmussen, R.M., Hall, W.D., 2008. Explicit Forecasts of Winter Precipitation Using an Improved Bulk Microphysics Scheme. Part II: Implementation of a New Snow Parameterization. Mon. Weather Rev. 136, 5095–5115. https://doi.org/10.1175/2008MWR2387.1

Turner, D.D., Vogelmann, A.M., Austin, R.T., Barnard, J.C., Cady-Pereira, K., Chiu, J.C., Clough, S.A., Flynn, C., Khaiyer, M.M., Liljegren, J., Johnson, K., Lin, B., Long, C., Marshak, A., Matrosov, S.Y., McFarlane, S.A., Miller, M., Min, Q., Minnis, P., O'Hirok, W., Wang, Z., Wiscombe, W., 2007. Thin Liquid Water Clouds: Their Importance and Our Challenge. Bull. Am. Meteorol. Soc. 88, 177–190. https://doi.org/10.1175/BAMS-88-2-177

Verlinde, J., Harrington, J.Y., McFarquhar, G.M., Yannuzzi, V.T., Avramov, A., Greenberg, S., Johnson, N., Zhang, G., Poellot, M.R., Mather, J.H., Turner, D.D., Eloranta, E.W., Zak, B.D., Prenni, A.J., Daniel, J.S., Kok, G.L., Tobin, D.C., Holz, R., Sassen, K., Spangenberg, D., Minnis, P., Tooman, T.P., Ivey, M.D., Richardson, S.J., Bahrmann, C.P., Shupe,

https://doi.org/10.5194/egusphere-2026-1486
Preprint. Discussion started: 24 March 2026

M., DeMott, P.J., Heymsfield, A.J., Schofield, R., 2007. The Mixed-Phase Arctic Cloud Experiment. Bull. Am. Meteorol. Soc. 88, 205–222. https://doi.org/10.1175/BAMS-88-2-205Xie, S. ARM Cloud Retrieval Ensemble Data (ACRED), 1999-01-01 to 2008-12-31, North Slope Alaska (NSA), Central Facility, Barrow AK (C1). Atmospheric Radiation Measurement (ARM) User Facility. https://doi.org/10.5439/1995948

Zhang, D. MWR Retrievals (MWRRET1LILJCLOU), 2001-04-01 to 2025-12-31, North Slope Alaska (NSA), Central Facility, Barrow AK (C1). Atmospheric Radiation Measurement (ARM) User Facility. https://doi.org/10.5439/1027369

Zhang, D. Data Quality Assessment for ARM Radiation Data (QCRAD1LONG), 1998-02-15 to 2026-03-15, North Slope Alaska (NSA), Central Facility, Barrow AK (C1). Atmospheric Radiation Measurement (ARM) User Facility. https://doi.org/10.5439/1027372